The sapphire (α-Al_2O_3) puzzle: Joint μSR and density-functional-theory study

R C Vilão,[1,*] A G Marinopoulos,[1] H V Alberto,[1] J M Gil,[1] J S Lord,[2] and A Weidinger[3]

[1] *University of Coimbra, CFisUC, Department of Physics, P-3004-516 Coimbra, Portugal*
[2] *ISIS Facility, Rutherford Appleton Laboratory, Chilton, Didcot, Oxon OX11 0QX, United Kingdom*
[3] *Department Spins in Energy Materials and Quantum Information Science (ASPIN), Helmholtz-Zentrum Berlin für Materialien und Energie, 14109 Berlin, Germany*

(Dated: October 17, 2021)

Sapphire (α-Al_2O_3) has been investigated by the muon spin rotation (μSR) method in several experiments in the past. The main μSR component is a diamagnetic-like signal with a fast relaxation. Because of this diamagnetic-like behavior, the signal was assigned to either positively charged muonium (Mu^+) or negatively charged muonium (Mu^-), but neither of the two assignments was satisfactory (the so-called "sapphire puzzle"). We have proposed that the signal is due to a weakly-paramagnetic muonium configuration (transition state) which is formed during the reaction of muonium with the host lattice. In the present paper we report new experimental data on Al_2O_3 and discuss these and earlier data in the Mu^- and in the transition state model. Calculations based on density-functional theory were also performed with detailed findings on the energetics of the different muonium configurations and their migration energies. We conclude that the transition state model is more plausible than the Mu^- model, but the Mu^- interpretation cannot be excluded completely. In addition, evidence is presented that the bare muon performs local motion but no long-range diffusion below room temperature in the microsecond time range.

PACS numbers:

I. INTRODUCTION

Sapphire (α-Al_2O_3) is an extremely versatile oxide material which is widely used as an excellent substrate for optical applications.[1] It is also being used or under consideration in many important applications in catalysis,[2] Li batteries,[3] emerging memories[4] or solar cells.[5,6] As with most oxide materials, Al_2O_3 can incorporate high concentrations of hydrogen, which can be as high as 1% in state-of-the-art atomic-layer deposition films.[7]

The importance of the hydrogen impurity in Al_2O_3 has been constantly pointed out in the literature, with a particular emphasis in its passivation effects or in its role as a compensating impurity.[8,9] The role of hydrogen two-level systems has also been pointed out, with possible high impact as a source of dissipation and decoherence in quantum computing materials.[10,11] However, the experimental detection of hydrogen is quite challenging. Muon spin spectroscopy and the modelling of hydrogen using muonium as light pseudo-isotope is therefore bound to bring crucial microscopic information on the hydrogen configurations and interactions inside Al_2O_3.

It is therefore not surprising that sapphire is one of the systems in muon-spin spectroscopy where muonium was first identified, both in longitudinal measurements[12] and in transverse measurements.[13] Actually, sapphire is the classical case where a muon spin rotation (μSR) signal is observed which shows a diamagnetic frequency behavior but relaxes more rapidly than expected for a diamagnetic configuration.[14–17] Fast-relaxing, diamagnetic-like signals were observed also in various other systems,[18–25] indicating that this is a quite common phenomenon of μSR in semiconductors and insulators.

The signal in Al_2O_3 was first interpreted as being due to Mu^+ which captures an electron from the ionization track after some delay (delayed muonium formation, see Ref. 15). Later, electric-field measurements showed that this interpretation could not be maintained and the signal was then tentatively assigned to Mu^- which loses the electron after some time.[16,26] Cox *et al.* mention that neither of the two assignments is really satisfactory and called it the sapphire puzzle.[17]

In a recent paper we suggested that this diamagnetic-like signal is actually paramagnetic with a hyperfine interaction which averages to almost zero.[27] We suggest that this signal is due to a transition state which is formed between the initial compact muonium in the pristine lattice and the final ground state muonium in the relaxed lattice.

The present paper contains new experimental data and an analysis of the present and previous data in the context of the Mu^- and transition state model. The designations Mu^+, Mu^0, and Mu^- are used for the different charge states of muon. Instead of Mu^+ we occasionally use μ^+ (bare muon) when this seems more natural in the context. We also include new results obtained with the aid of first-principles calculations for hydrogen based on density-functional theory.[28,29] These calculations resolved the energetics of the three different hydrogen states, H^+, H^0, and H^- and their preferred sites in the oxide lattice. The respective defect transition levels and migration-energy profile for the neutral H^0 state were also determined. Most of these calculations accessed the ground-state energies and bonding properties of hydrogen which should be nearly identical to the ones of the lighter muon particle.[30,31] If isotope effects play a role, this is specifically noted.

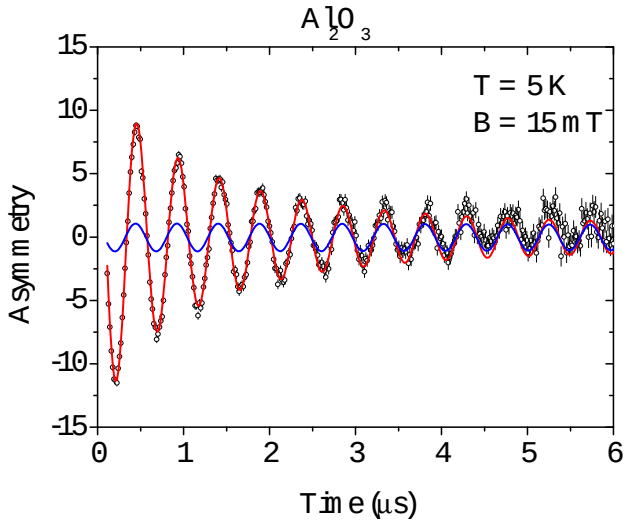

FIG. 1: Transverse-field μSR time spectrum of α-Al_2O_3 at $T = 5$ K and $B = 15$ mT. The spectrum is fitted with a fast and slowly relaxing component. The blue line shows the slowly relaxing component and the red line the total asymmetry.

II. EXPERIMENTAL DETAILS AND RESULTS

Muon spin rotation measurements were performed at the ISIS Facility of the Rutherford Appleton Laboratory in Chilton, UK. The measurements were performed in transverse geometry, in order to take advantage of the better definition of parameters provided by the muon spin oscillations. The experiments took place in the EMU spectrometer and an applied magnetic field B = 15 mT was used. A flypast setup was used in order to reduce background.[32] Calibration of the maximum instrumental asymmetry was done through a measurement with silver. Data analysis was performed using the WiMDA program.[33]

A commercial high-purity α-Al_2O_3 monocrystalline sample, acquired from the MTI corporation was used. The sample was cut in the $c-$plane, so that the $c-$axis was parallel to the initial spin polarization of the incoming muon beam.

Figure 1 shows a transverse-field ($B = 15$ mT) μSR time spectrum at $T = 5$ K. The frequency corresponds to the muon Larmor frequency but the relaxation is not uniform; clearly a fast and an almost non-relaxing component are seen.

For a first survey, the data were fitted with the two-component precession formula

$$A(t) = A_f \exp(-\lambda_f t)\cos(2\pi\nu_f t + \phi_f) + \\ + A_s \exp(-\frac{1}{2}\sigma_s^2 t^2)\cos(2\pi\nu_s t + \phi_s) \quad (1)$$

where A_f and A_s are the precession amplitudes of the fast relaxing and of the slow relaxing component, respectively; λ_f and σ_s are the respective relaxations, where a lorentzian shape was used for the fast component and a gaussian shape was selected for the slow component, as will be discussed later. ν_f and ν_s are the respective precession frequencies and ϕ_f and ϕ_s the corresponding initial phases of precession. The maximum instrumental asymmetry A_{max} at these measurements was determined from a calibration with silver, which therefore allowed to determine the fraction of muons associated to each component as $f_s = A_s/A_{max}$ and $f_f = A_f/A_{max}$.

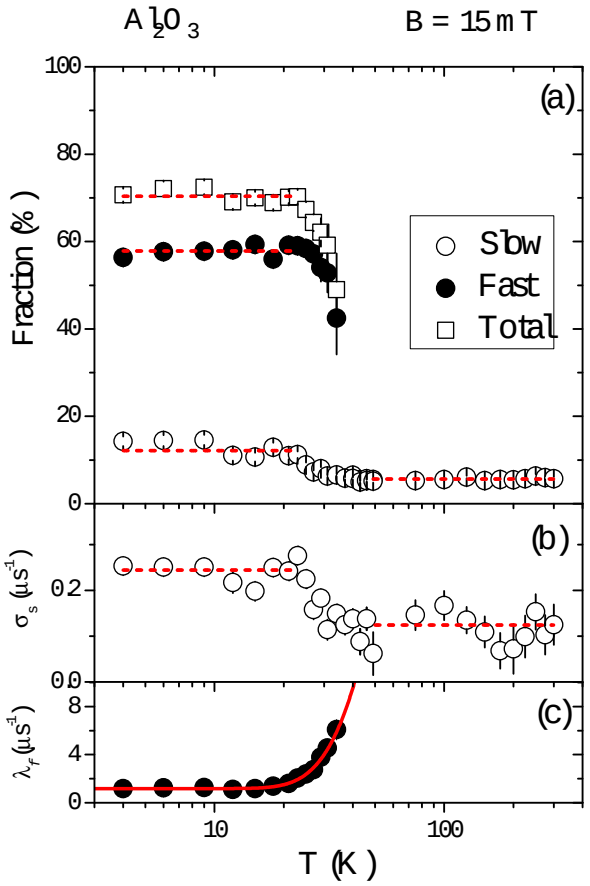

FIG. 2: μSR fractions (a) and relaxation rates (b) and (c) of a transverse-field measurement in Al_2O_3 at $B = 15$ mT. The dashed lines in (a) and (b) are guides to the eye, the solid lines in (c) is a fit with Eq. 2.

All parameters were left free for this survey. The results as a function of temperature are shown in Fig. 2 and in Fig. 3.

In the low temperature region (below 40 K), two differently relaxing components can be distinguished: a slowly relaxing part with $\sigma \approx 0.25\,\mu s^{-1}$ and a fast relaxing part with $\lambda \approx 1.2\,\mu s^{-1}$. The total diamagnetic-like signal amounts to about 70% and is approximately constant up to about 25 K and starts to decrease thereafter. The decrease is due to μSR related effects (see below) and

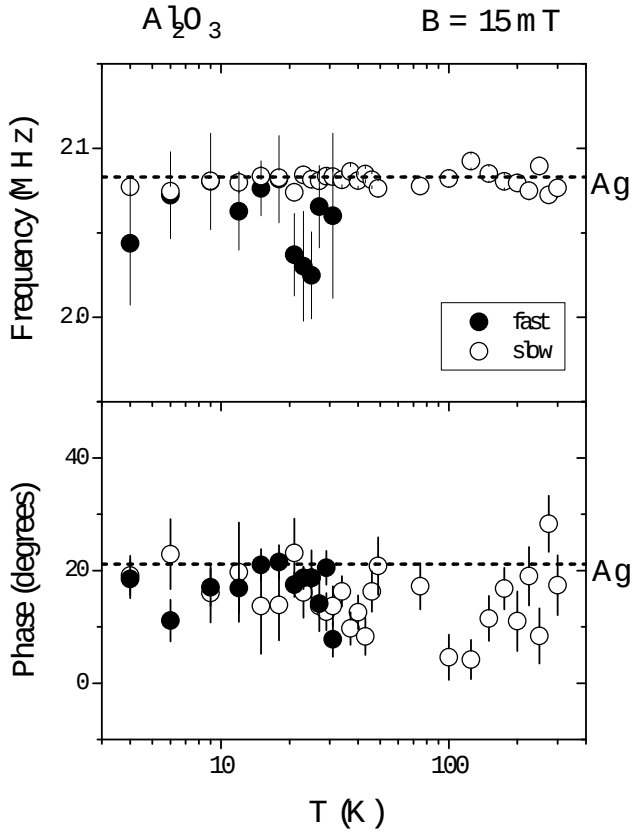

FIG. 3: Frequency and phase of the fast (dots) and the slowly (open circles) relaxing signal obtained from the fit to the transverse field data (B = 15 mT). The dotted lines correspond to the calibration with an Ag sample.

not to changes in the sample. Thus, the missing fraction amounts to approximately 30%.

The relaxation rate of the slow component decreases in the temperature range between 30 and 40 K from about $0.25\,\mu\mathrm{s}^{-1}$ to about $0.12\,\mu\mathrm{s}^{-1}$. We assign the $0.12\,\mu\mathrm{s}^{-1}$ relaxation above 40 K to the bare-muon behavior. Below 40 K, both the fraction and the relaxation of the slow component increase. This may be due to a change of the bare-muon behavior, but it could also be due to a third component which has to be added to the fast-relaxing fraction. We will address this point later.

The relaxation rate of the fast component was fitted with the function

$$\lambda(T) = \lambda_0 + \lambda_1 \exp\left(-\frac{E_a}{kT}\right) \qquad (2)$$

where $\lambda(T)$, λ_0 and λ_1 refer to relaxation rates, E_a to the activation energy and k to the Boltzmann constant. The fit yields: $\lambda_0 = 1.18(3)\,\mu\mathrm{s}^{-1}$, $\lambda_1 = 216(72)\,\mu\mathrm{s}^{-1}$ and E_a = 11.2(9) meV (solid line in Fig. 2 (c)). The pre-exponential factor is small compared to phonon frequencies. This may be due to tunneling of the light particle or dynamical effects directly after the formation of the state may also contribute to the conversion. The present results are in agreement with previous data from a zero-field measurement where the signal was seen up to room temperature and activation energy of about 10 meV is reported.[15]

Frequency and phase in Fig. 3 correspond over the most part of the temperature range to the calibration values obtained with an Ag sample. The apparent dip in the phase shift around 100 K is not confirmed in a more detailed one-component analysis as seen in Fig. 4 A small frequency shift of the fast component is noticed only around 30 K to 40 K. Unlike what we observed in Ref. 27, the magnetic field here is too large in order to observe a significant shift.

As can be seen from Fig. 2, the parameters of the signal change strongly in the temperature region around 20 to 40 K. This indicates that different processes dominate in the low and high temperature region. We will therefore discuss these regions separately.

A. Data from 40 to 300 K

In the temperature region from 40 to 300 K, only the slowly relaxing component is seen. The background contribution to the signal is negligible in these measurements using the fly-past setup.[32] The fast component which has been seen in a zero-field experiment up to room temperature[15] is not observable in the present transverse field experiment due to dephasing. We have analyzed the data above 40 K with a one-component fit, using a Gaussian $\left(\exp\left(-\sigma^2 t^2/2\right)\right)$ relaxation function. The fit data are displayed in Fig. 4.

As can be seen from Fig. 4, all four parameters are constant within experimental errors. The fraction amounts to approximately 5.8% of all muons and the relaxation rate is approximately $\sigma \approx 0.12\,\mu\mathrm{s}^{-1}$. The frequency and phase correspond to the calibration values. We assign the observed signal between 40 and 300 K to diamagnetic μ^+. The implications of the observed relaxation values will be discussed in section IV C.

B. Data below 40 K

In the preceding analysis (Fig. 2) the signal was split into a fast and a slow component. The slow component shows a peculiar behavior below 40 K: both the fraction and the relaxation increase and saturate at higher values. A possibility is that this reflects a change of the bare muon behavior, e.g. localization at a specific site while at higher temperatures some averaging occurs. We will discuss that later in connection with local averaging. However, the fact that not only the relaxation but also the

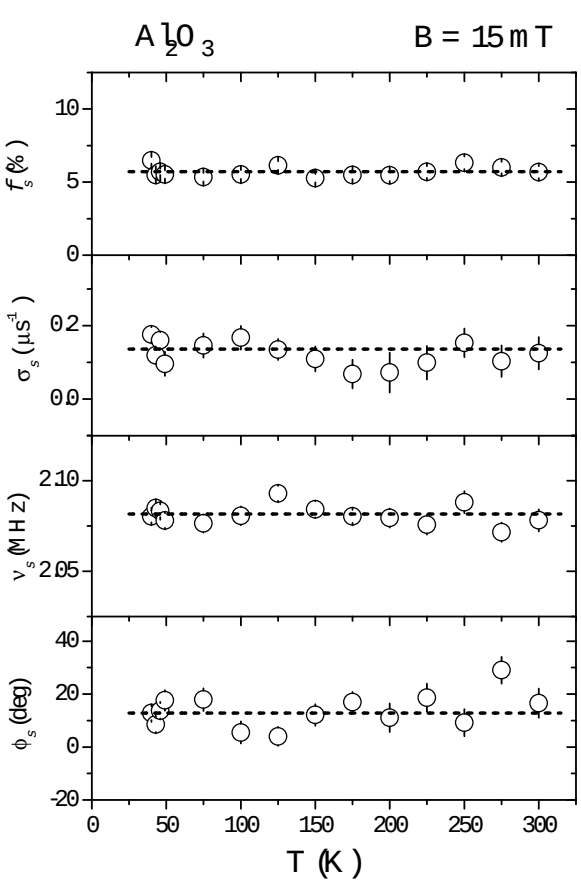

FIG. 4: Fit parameters of the slowly relaxing signal in Al_2O_3 above 40 K (Gaussian relaxation, $B = 15$ mT). The horizontal lines indicated the average values. For the frequency and the phase they correspond to the calibration values.

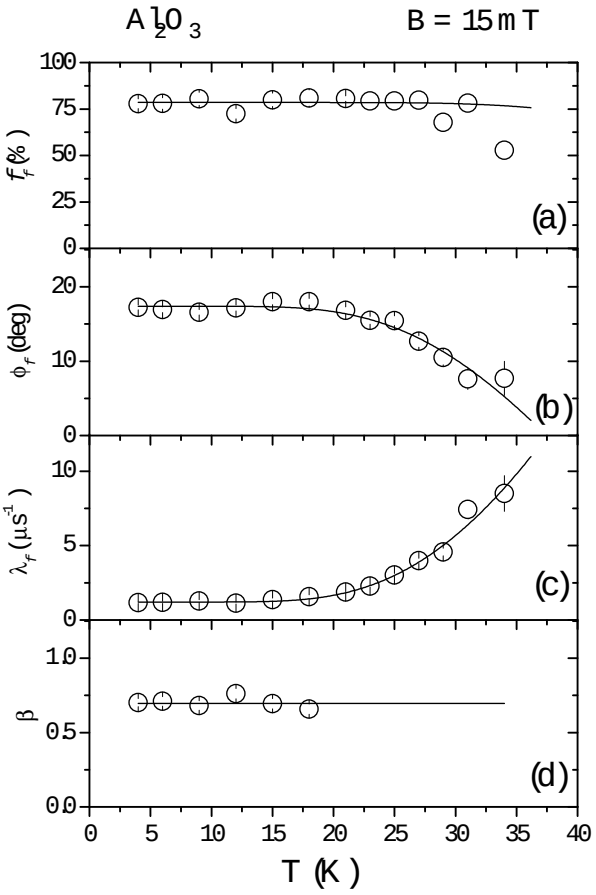

FIG. 5: Fit parameters of the fast component with a stretched exponential function for the relaxation $\left(\exp\left[-(\lambda t)^{\beta}\right]\right)$. The fraction f_f and phase ϕ_f are correlated via the dephasing formula Eq. 3; the solid lines in (a) and (b) correspond to a common fit to the data. The solid line in (c) is a fit to the relaxation λ_f with an activation function (Eq. 2) and the solid line in (d) is a guide to the eye. For temperatures above 18 K, the stretching parameter β was fixed to the value at lower temperatures.

fraction increases makes this interpretation questionable since a temperature-independent fraction is expected if the slow fraction stems from the charge exchange regime. We therefore attribute this extra fraction to the fast part of the signal.

A three-component analysis of the signal leads to too large ambiguities, and we have therefore adopted the following procedure: The parameters of the slow component were fixed to the values obtained above 40 K. The rest was fitted with only one component but with a stretched exponential function $\left(\exp\left[-(\lambda t)^{\beta}\right]\right)$. The stretched exponential simulates approximately the superposition of two exponential functions with slightly different relaxations. But it may also describe the physical situation where the signal is not purely exponential but has a tail. In the fitting function, a correlation between the fraction and the phase is included (see description below). The fit results are displayed in Fig. 5.

The fast component disappears above 40 K because of too large relaxation. However, between 30 and 40 K, where the signal is still observable, a reduction of the amplitude and a significant phase shift are observed. The phase shift in the 30 to 40 K region is seen also in Fig. 3 but is there less pronounced. The reason is a different partition between the fast and the slow component. In Fig. 3 the slow component not only contains the diamagnetic fraction, which has no phase shift, but also a contribution from the paramagnetic part, with a phase shift. Therefore, both signals in Fig. 3 indicate a slight phase shift but which is less pronounced than that in Fig. 5, where the shift for the full paramagnetic part is shown. The statistical fluctuations in Fig. 5 are smaller than in Fig. 3 since fewer free parameters are fitted. The phase shift and the relaxation in Fig. 5 are not correlated since they refer to different processes, the phase

shift being caused by the delayed formation of the observed state and the relaxation by the lifetime of this state. These effects in amplitude and phase indicate that the fast relaxing component is formed with some delay from a precursor.[34]

We have fitted the fast fraction f_f and the phase shift $\Delta\phi$ with

$$\begin{aligned} f_f &= \frac{f_f^0}{\sqrt{1+(\Delta\omega\,\tau)^2}} \\ \Delta\phi &= \arctan(\Delta\omega\,\tau) \end{aligned} \quad (3)$$

where $\Delta\omega$ is an effective frequency difference and τ the conversion time.[34] The result of a common fit to both parameters is shown as lines in Fig. 5 (a) and (b). The functional dependence has no significance because of the scarcity of the data, but the numerical values of the parameters shall be discussed shortly.

It is remarkable that the phase shift occurs at somewhat elevated temperatures but is not seen at the lowest temperatures. This indicates that the conversion is faster at low than at higher temperatures, contrary to what one expect for a thermally activated process. We suggest that at low temperatures an extra energy from the stopping process accelerates the conversion. Such inverse temperature behavior has been observed also in other experiments and has been attributed to a thermal spike at the muon stopping site.[35]

The phase shift of about 15 degrees at 35 K corresponds to $\Delta\omega\,\tau = 0.27$. In the present case of the conversion of atomic muonium (with an hyperfine interaction at approximately the vacuum value) to an almost diamagnetic state at low field, $\Delta\omega$ adopts roughly only two values, either that of the hyperfine transition, i.e. $\Delta\omega_0 = 2\pi\nu_0 \approx 28$ rad.ns^{-1} or that of the inter-triplet transition at 15 mT, i.e. $\Delta\omega_{12} = 2\pi\nu_{12} \approx 13$ rad.μs^{-1}, both with approximately the same amplitude.[30]

However, the observed dephasing cannot be due to the low frequency $\Delta\omega_{12}$ difference. In fact, dephasing due to the concomitant high frequency $\Delta\omega_0$ would cause a complete disappearance of half of the corresponding fraction of muon spin polarization. This is inconsistent with the experimental observation of 60% of the muon spin polarization, whereas less than 30% of the fraction is missing. This implies that the effective contribution to the dephasing is $\Delta\omega_0 = 28$ rad.ns^{-1}. Inserting this value in $\Delta\omega\,\tau = 0.27$ yields $\tau \approx 10$ ps, i.e. a conversion time from atomic muonium to diamagnetic-like state well below 1 ns. We note that the measured phase shift is the resulting shift of two components where one has no phase shift. Thus the quoted value is only an order of magnitude estimate of the conversion time.

The relaxation rate of the fast component in Fig. 5 (c) shows the same behavior as in Fig. 2 but the fit values obtained with Eq. 2 are slightly different due to the use of the stretched exponential function. We obtain here $\lambda_0 = 1.21(4)\mu$s^{-1}, $\lambda_1 = 36(4)\mu$s^{-1} and $E_a = 11.9(7)$ meV (solid line in Fig. 5 (c)). Assuming that λ_0 is due to hyperfine broadening, the average hyperfine interaction is approximately $A \approx \lambda_0/\pi \approx 0.39$ MHz. A hyperfine-broadened line has not necessarily lorentzian shape and thus could explain the deviation of the relaxation from the pure exponential form ($\beta \neq 1$).

III. DENSITY FUNCTIONAL THEORY CALCULATIONS

A. Theoretical background and preliminaries

The first-principles calculations in the present study were based on spin-polarised density-functional theory[28,29] and the projector augmented-wave (PAW) method,[36,37] as implemented in the VASP code.[38–40] Core-valence interactions were represented by pseudopotentials with the valence states expanded using a plane-wave basis. The size of this basis was controlled by the kinetic energy cutoff which was set at 480 eV. For exchange-correlation effects two different methodologies were employed. First, the semilocal PBE functional[41] which is based on the generalized-gradient approximation (GGA) for exchange and correlation. The second approach was the HSE06 hybrid functional[42,43] which includes exact screened exchange with a portion of non-local Fock exchange admixed to the semilocal PBE exchange. A fraction, α, equal to 0.37 of exact exchange was found to reproduce the experimental electronic gap of sapphire and was chosen for all defect calculations with the HSE06 functional.

Sapphire (α-Al_2O_3) is a wide-gap oxide with a structure composed of an approximately hexagonal closed-pack (*hcp*) arrangement of oxygen ions with the smaller aluminum cations occupying two-thirds of the available octahedral interstices.[44] Crystallographically the α phase is described by a rhombohedral space group ($R\bar{3}c$) which is represented by a trigonal primitive unit cell of ten atoms. In the present study the optimum lattice parameters of the sapphire lattice were determined through energy minimization of the non-primitive 30-atom hexagonal cell adopting a Γ-centered 4×4×2 **k**-point mesh. The resulting lattice parameters were found equal to: a=4.80 Å and c=13.11 Å, when using the PBE functional. These values slightly overestimate the experimental results for the a and c parameters, which were reported to be 4.76 Å and c=12.99 Å, respectively.[45] The structural optimization of the bulk cell with the hybrid HSE06 functional led to $a = 4.73$ Å and $c = 12.92$ Å.

The defect calculations were performed by means of a supercell approach and three-dimensional periodic boundary conditions. 120-atom bulk-crystalline supercells were constructed after doubling the dimensions of the hexagonal unit cell along the **a** and **b** lattice vectors on the basal plane. A broader, 2×2×2, **k**-point mesh was used for these cases.

The formation energies $E_{\rm form}(H^q)$ of all possible hy-

drogen configurations in their charge states q (q=–1, 0 and +1) were determined as a function of the electron chemical potential (Fermi level $E_{\rm F}$) in the gap:

$$E_{\rm form}(H^q) = E_{\rm tot}(H^q) - E_{\rm tot}({\rm bulk}) - \mu_H + q(E_{\rm F} + E_{\rm V}) \quad (4)$$

$E_{\rm tot}(H^q)$ is the total energy of the supercell with a single hydrogen present in the charge state q, and $E_{\rm tot}$(bulk) the total energy of the perfect-crystal supercell. $E_{\rm V}$ is the energy of the valence-band (VB) top of the perfect-crystal supercell and sets the reference energy for the Fermi-level positions in the electronic band gap. The formation energies also depend upon the chemical potential of hydrogen, μ_H. Electrostatic corrections due to image interactions for H^+ and H^- were also included according to the scheme of Makov and Payne.[50] These amounted to 0.19 eV, considering an average dielectric constant of 10, as reported in existing experimental studies for the α phase of the aluminum oxide.[51]

The charge-transition levels, (q/q'), of hydrogen are defined as the values of the Fermi level in the gap where the formation energies of the two different charge states, $E_{\rm form}(H^q)$ and $E_{\rm form}(H^{q'})$ are equal. All the (q/q') levels reported in the present study were obtained by means of the hybrid HSE06 functional, unless noted otherwise. The electronic gap of sapphire determined by HSE06 is equal to 9.31 eV. This magnitude is consistent with experimental measurements[46,47] and results of previous calculations performed by means of the hybrid PBE0 functional[48] and the GW perturbative approach.[49]

The calculations of the second-order hyperfine tensor $\mathbf{A}_{\rm ij}$ were performed using a formalism which includes core spin polarization effects.[53] Since the main aim in the present study has been to characterize paramagnetic defects the quantity of interest was the isotropic (Fermi-contact) part of this tensor, $A_{\rm iso}$. This part is a measure of the localization of the electron of hydrogen (muonium). More specifically, $A_{\rm iso}$ is proportional to the magnitude of the electron spin density, ρ_s (ρ_s = $\rho_\uparrow$ - $\rho_\downarrow$) at the hydrogen (muon) site, $\mathbf{R}$, and is obtained as:[54]

$$A_{\rm iso} = \frac{8\pi}{3}\, g_e \mu_e g_H \mu_H \rho_s(\mathbf{R}) \quad (5)$$

where: g_e is the electron g-factor, μ_e the Bohr magneton, g_H the hydrogen nuclear gyromagnetic ratio and μ_H its nuclear magneton.

The migration paths for hydrogen and corresponding energy profiles were determined from the nudged elastic-band (NEB) method.[52] From these results the classical migration barriers for hydrogen motion in the lattice were deduced. Quantum effects originating from the zero-point motion of hydrogen (and muonium) were determined for specific cases along the final migration paths, and are discussed in more detail in section IV B.

B. Hydrogen configurations and defect levels

Hydrogen was inserted interstitially at various sites inside the oxide lattice and energy minimization was then performed with respect to individual atomic displacements. All stable hydrogen configurations that were found correspond to energy minima in this minimization procedure.

The present findings on the final lowest-energy hydrogen states agree with previous first-principles calculations.[11,55] Hydrogen in its positively-charged state, H^+, was observed to interact rather strongly with the host lattice. It binds to oxygen ions and forms hydroxide-ion (O-H) configurations (see Fig. 6(a)). These bound configurations consist of a short covalent O-H bond, with a bond length equal to 1.01 Å. Hydrogen also remains close to a second nearest oxygen neighbor from the adjacent basal plane, denoted by the symbol X in Fig. 6(a). The distance to this oxygen ion is 1.67 Å. In contrast, hydrogen in its neutral, H^0, and negatively-charged H^- states, was found to reside most favorably at the empty octahedral interstitial sites of the lattice (see Fig. 6(b)). In the octahedral interstitial site the hydrogen has six oxygen neighbors; three from each of the adjacent basal planes. These ions define an O-cage which surrounds the impurity. Furthermore, the two Al ions from the cation column along the crystallographic **c** axis are also found very close to the hydrogen nucleus; the corresponding H–Al distances in the H^0 state are equal to 1.89 Å. In the H^- state the two positively-charged Al ions are drawn closer to hydrogen, owing to the mutual electrostatic attraction, and the H–Al distances are smaller (1.63 Å).

The bond-type (bound) configuration was also found to be stable for H^0, albeit with a higher energy. Calculations using the semilocal PBE functional showed that this configuration has an excess of 1.43 eV with respect to the H^0 ground state (interstitial configuration). The calculation of the spin density of H^0 in the bound configuration showed that the excess electron is very delocalized (see Fig. 6(c)); it can be seen that the spin density extends virtually to the whole supercell. Calculations of the hyperfine interaction using the semilocal PBE functional led to an isotropic $A_{\rm iso}$ (Fermi-contact) term of zero magnitude.

In contrast, corresponding calculations for H^0 occupying the interstitial site showed that hydrogen possesses a strong atom-like character with the electron density centered at the hydrogen nucleus (see Fig. 6(d)). The density is very compact and symmetric, although a deviation from spherical symmetry is also evident, a consequence of the crystalline anisotropy of the local envinonment. A finite spin-density spilling to the six nearest oxygen neighbors also takes place, suggesting that hydrogen incorporation in this site polarizes its immediate environment. Calculations of the hyperfine tensor for this configuration within the GGA led to a high Fermi-contact term, $A_{\rm iso}$, with a magnitude of 1320 MHz ($\approx$ 93% of the vacuum

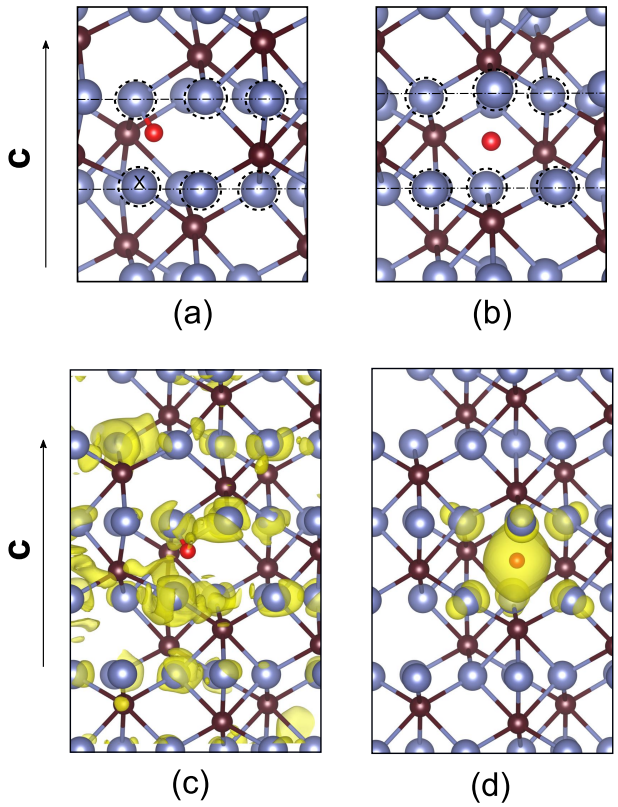

FIG. 6: Distinct hydrogen configurations in the sapphire lattice and calculated electron-spin density isosurfaces for the neutral charged states. The view is perpendicular to the crystallographic **c** axis, and along the basal planes (denoted by the horizontal dashed-dotted lines). (a) Bond-type bound hydrogen configuration. (b) Hydrogen occupying an octahedral interstitial site. (c) Spin density (in yellow) of the higher-energy H^0 bound configuration. Isosurface value set at 2×10^{-9} e/Å^3. (d) Spin density (in yellow) of the ground-state H^0 interstitial configuration. Isosurface value set at 4.4×10^{-3} e/Å^3. The various chemical elements are represented as follows: Al by the smaller brown spheres, O by the larger blue spheres and H by the small red sphere. The six nearest oxygen ions to hydrogen are denoted by the dashed circles.

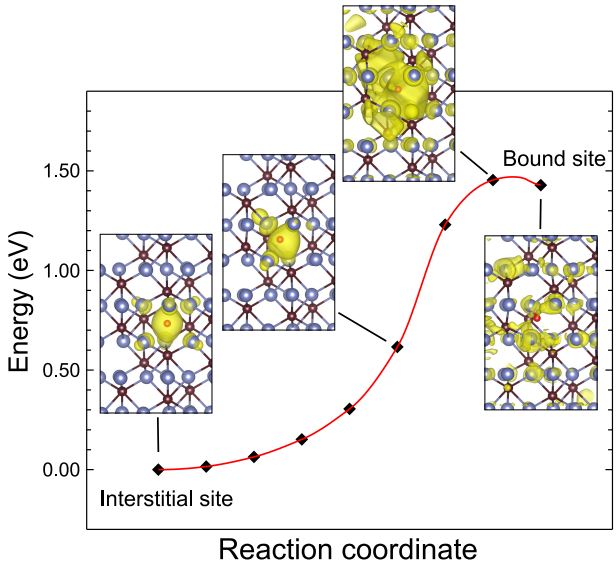

FIG. 7: Energy profile of the migration of neutral hydrogen along the minimum-energy path (MEP) that connects the interstitial and bound sites. Atomistic structures and electron-spin densities for the initial, final and two intermediate configurations are shown explicitly. The filled diamond symbols represent the exact results from the NEB optimization. The calculations were carried out using the semilocal PBE functional.

value).

Further calculations were also performed in order to probe the energy landscape between the two distinct neutral configurations of hydrogen. A migration pathway between the interstitial (ground-state) and higher-energy bound states was traced and the corresponding energy profile was determined by means of the NEB method. The final result is depicted in Fig. 7 and it shows the final minimum-energy path obtained from the NEB optimization. It can be seen that the hydrogen atom diffusing from the interstitial site has to overcome an energy barrier of 1.47 eV in order to access the bound site. On the other hand, when hydrogen finds itself at the bound site it only needs to surmount a very small detrapping barrier of about 40 meV in order to migrate towards the lower-energy interstitial site. The way these findings affect the dynamic behavior of muonium will be discussed in more detail in section IV B.

The evolution of the electron density was also examined along the connecting NEB path. For two intermediate configutations the corresponsing spin densities are plotted (see Fig. 7). It is evident that the electron density becomes more delocalized when the hydrogen migrates away from the interstitial site and approaches the bound site. The largest change is recorded close to the saddle point of the path whereby the excess electron starts to spill outside the oxygen cage which initially surrounds the migrating hydrogen atom in the ground state.

The donor (+/0) and acceptor (0/−) levels for hydrogen were determined from the hybrid-functional (HSE06) approach by taking the lowest-energy configurations for each charge state, namely the interstitial configurations for H^0 and H^- and the bound for H^+. These charge-transition levels are shown in Fig. 8. It can be seen that they lie deep inside the gap, and considerably far away from both the valence-band and conduction-band edges, E_V and E_C, respectively. More specifically, the acceptor level is found at: $(0/-) = E_V + 5.67$ eV, and the donor level at: $(+/0) = E_C - 2.57$ eV. Furthermore, the donor

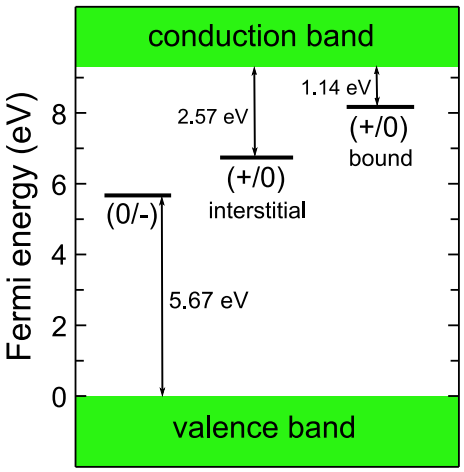

FIG. 8: Positions of the charge-transition levels of hydrogen inside the band gap. The results were obtained from the hybrid-functional (HSE06) approach. The position of the donor level, (+/0), for the higher-energy bound configuration was determined from calculations using the semilocal PBE functional. The reference energy is set at the valence-band edge, E_V.

level, (+/0), associated with the higher-energy neutral bound configuration is also shown. It lies much closer to the conduction band edge: (+/0) = E_C – 1.14 eV. The specific position of its energy was approximated by calculating the energy difference from the H^0 ground state by means of the PBE functional.

IV. DISCUSSION

We should first mention an earlier high-field experiment in which ground state atomic muonium has been observed with a fraction of 10%.[13] The experimental hyperfine interaction is very large (99% of the vacuum value) and corresponds very well to the theoretical value for ground state H^0 (93% of the vacuum value). The deviations are well within experimental and theoretical uncertainties originating from anisotropy and motional averaging effects or the use of the GGA approximation.[53,54,56] In the present low-field experiment, atomic muonium is not observed because of dephasing. The corresponding fraction is contained in the missing fraction, which makes up about 30% in total.

The diamagnetic (μ^+) fraction (about 5.8%) will be discussed at the end of this section. The main part of the discussion concerns the fast relaxing signal for which competing interpretations have been proposed. We will analyze the data in the "Mu^- model" and in the "transition state" model, respectively. In both models the starting configuration is atomic muonium at an interstitial site in the pristine lattice. The electron stems from the pickup in the charge exchange regime or is captured shortly before the muon stops.

The atomic oxygen cage of the sapphire lattice plays a central role in the present analysis. This is centered on the empty octahedral interstices of the lattice and is composed of the six nearest oxygen atoms which are arranged in two groups of three in the two adjacent basal planes (see Fig. 6). It is assumed that the muon is either located in the center of this cage (interstitial configuration) or bound to an oxygen atom (bound O−Mu configuration). These two configurations are shown in Fig. 6.

TABLE I: The three consecutive reactions are: i) Relaxation of the lattice around muonium $\left(Mu^{0*} \rightarrow Mu^0\right)$, ii) capture of an electron from the conduction band $\left(Mu^0 + e^- \rightarrow Mu^-\right)$, and iii) capture of a hole from the valence band $\left(Mu^- + h^+ \rightarrow Mu^0\right)$. The first two reactions are prompt on the µSR time scale whereas the third is delayed at low temperature by about 1 μs. The numerical values in column 3 and 4 are from the DFT calculations described in section III.

Reaction	Conversion time	Energy release	Cage volume change	Driving process
$Mu^{0*} \rightarrow Mu^0$	Prompt	0.15 eV	+10%	Stress release
$Mu^0 + e^- \rightarrow Mu^-$	Prompt ($<$ 1 ns)	3.64 eV	+15%	Capture of a radiolytic electron
$Mu^- + h^+ \rightarrow Mu^0$	Delayed ($\approx$ 1 μs)	5.67 eV	-15%	Capture of a radiolytic hole

A. Mu^- model

In this model, the fast-relaxing diamagnetic-like signal is assigned to Mu^-. The relaxation is due to the loss of an electron, i.e. the conversion of diamagnetic Mu^- to paramagnetic Mu^0. The sequence of reactions which characterize this signal is summarized in Table I.

The first step is the formation of ground state muonium by the relaxation of the lattice around muonium when the latter occupies the interstitial site. This seems a rather simple process whereby the lattice relaxes isotropically: the calculated energy release determined by the semilocal PBE functional is only 0.15 eV and the volume expansion of the oxygen cage by about 10% is plausible. The formation of the ground state competes with the formation of the transition state, as discussed in the next subsection (IV B).

The next step is that ground state muonium captures an electron from the ionization track (no conduction electrons exist in the native material). Dephasing considerations in the experimental section indicates that the process has to occur in the sub-nanosecond time range. The likelihood of such a capture process can hardly be estimated at present. Storchak *et al.* mention capture rates at Mu^+ in Al_2O_3 in the order of 1 per μs at low temperatures.[15] Although the interpretation of their data is questionable,[16,57] such rates have been presented as reasonable in Ref. 58. In the present case the capture rate would have to be at least three orders of magnitude faster (1 per ns instead of 1 per μs), making prompt Mu^- formation not very likely.

The final disappearance of the signal (after about 1 μs at low temperatures) is assigned in this model to the loss of an electron. Since the acceptor level, $(0/-)$, lies deep in the gap (approximately 3.5 eV below the conduction band edge, Fig. 8), electron promotion to the conduction band is not possible. Thus, the only possibility is the recombination with a hole in the valence band. Here again, the only candidates are holes from the ionization track. These holes need to have survived recombination with electrons in the track and have to arrive with sufficient probability at the Mu^- site, in spite of diffusion in all directions. This process seems not very likely, although it cannot be definitively excluded.

B. Transition state model

In this model, one assumes that the incoming muonium forms an intermediate configuration with an almost diamagnetic-like behavior. We assume that muonium is finally stopped at the top of the transition barrier since only there the residence time is sufficiently long for lattice relaxation. The crossing of the potential minimum region, e.g. for a muonium atom with a kinetic energy of 1 eV, takes only about 10^{-14} s, a time too short for the excitation of typical Debye phonons with a period of 10^{-13} s. The resulting state corresponds to the bound configuration and, in the present Al_2O_3 case, we identify this transition state with the hydroxide-like bound configuration described in section III. In this configuration the electron of muonium is strongly delocalized with vanishing weight at the proton/muon site (Fig. 6 (c)). DFT-GGA calculations give very small values for the Fermi-contact term (in the order of a few kHz, considerably smaller than the values calculated in ZrO_2).[24,27,59] The dipolar interaction averages to almost zero due to the distribution of the electron in all directions around the muon. There is also some dynamics possible (electron jumps) which cause also a reduction of the average dipolar interaction. Therefore, the apparent μSR frequency corresponds to the Larmor frequency.

The DFT-GGA calculations place the formation energy of the neutral O−H like bound state at 1.43 eV above the Mu^0 ground state (Fig. 6 (d)). Thus, the energy release by lattice relaxation (calculated to be 0.15 eV) is not sufficient for muonium initially at the interstitial site to overcome the large barrier and to reach the bound state. However, a much larger energy is available from the stopping process. At the end of the trajectory, muonium is slowed down to an energy which is just sufficient to surmount the diffusion barrier. At the top of the barrier, the kinetic energy is low and muonium has sufficient time to react with the lattice and form a bound state.

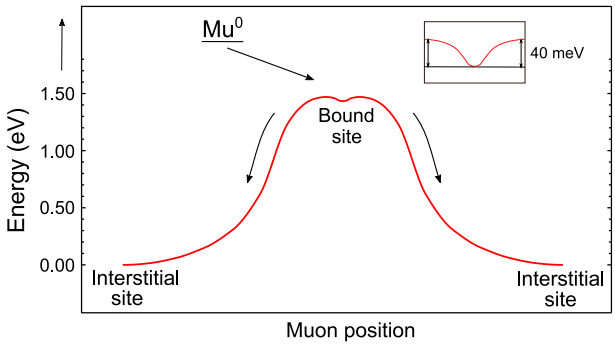

FIG. 9: Formation and decay of the intermediate O−Mu configuration (transition state) at the bound site in Al_2O_3. An incoming muonium (Mu^0) is slowed down and trapped at a local energy minimum at the top of the diffusion barrier. The energy profile (red curve) for the transition from the metastable bound state to ground-state muonium at a neighbouring interstitial site corresponds to the calculated NEB curve shown in Fig. 7. The insert shows the shallow energy minimum ($\approx$ 40 meV) at the top of the barrier.

The DFT calculations (Fig. 9) show that at the top of the diffusion barrier a local minimum exists if H^0 (Mu^0) passes by an oxygen atom; H^0 (Mu^0) is attracted to this atom and a metastable state with a delocalized electron distribution is formed. We identify this state with the transition state in the transition state model.

The bound O−Mu configuration is unstable and converts by thermal activation to ground state muonium at an interstitial site. The value of the activation energy for this process can be obtained experimentally from the increase of the fast relaxation rate with temperature if one assumes that this increase is due to the lifetime of the transition state. The experimental activation energy derived from this measurement is approximately 11 meV (Fig. 2 and Eq. 2).

This value corresponds very well to the depth of the local minimum of about 40 meV as determined from the NEB calculations using the PBE functional (see Fig. 9). The difference is not significant considering the numerical uncertainties of the NEB results as well as zero-point motion effects. Zero-point energies at the bound-state and saddle-point sites (see Fig. 9) have been estimated within the harmonic approximation using the muon isotopic mass. They were found to differ by less than 40 meV. These findings confirm the consistency of the experimental and theoretical activation energy.

C. Muon position and local motion

The relaxation rate of the slow component (Fig. 4 (b)) is approximately constant from 40 K to 300 K and has a value of $\sigma \approx 0.12\ \mu s^{-1}$. The relaxation rate does not decrease to zero with increasing temperature, indicating that below 300 K, no long range diffusion takes place in the microsecond time range. However, local site changes leading to a partial reduction of the average interaction can be inferred from the data, as discussed below.

The μ^+ spin relaxation is due to the magnetic interaction of the muon spin with the nuclear moments of the surrounding ^{27}Al atoms (the O atoms do not contribute) and can be calculated using the known equation:[60,61]

$$\sigma^2 = \gamma_\mu^2 \sum_j \left(\frac{\mu_0}{4\pi}\right)^2 I\,(I+1)\,\hbar^2 \gamma_{N,j}^2 \frac{\left[1-3\cos^2(\theta_j)\right]^2}{r_j^6} \tag{6}$$

where μ_0 is the magnetic permitivitty of vacuum and γ_μ and $\gamma_{N,j}$ are, respectively, the gyromagnetic ratios of the muon and of the ^{27}Al nucleus (with spin $I = 5/2$) at position $\vec{r}_j$ with respect to the muon; θ_j is the angle between $\vec{r}_j$ and the applied magnetic field.

The atomic positions were taken from the DFT calculations for the bound O−H^+ configuration as depicted in Fig. 6 (a). The magnetic field orientation was perpendicular to the c−axis of the hcp Al_2O_3 sample, and was either along the a-axis or perpendicular to it. The experiment was not originally designed as an orientation-dependent study, so the precise orientation of the external magnetic in the c-plane is not known. This is however of little importance, since the relaxation values for the two possible orientations are very similar.

The calculated relaxation rates for these two directions are 0.33 μs^{-1} and 0.35 μs^{-1}, respectively. These values are almost a factor of three larger than the experimental value of 0.12 μs^{-1}. Thus, considerable motional averaging takes place. Gordon *et al.* proposed that a resonating state between two hydrogen positions is formed.[11] The two positions correspond to the bound configuration at two adjacent oxygen atoms. The nuclear dipolar interaction at the two sites is different and therefore averaging leads to a reduction of the μSR relaxation rate, as observed experimentally. Our data do not allow a distinction between a resonating situation and fast jumping between the two sites.

In the experimental section, we mentioned that the relaxation rate of the slow component increases below 40 K and reaches a value of $\sigma \approx 0.25\ \mu s^{-1}$ (Fig. 2 (b)). It could be possible that this increase is due to the localization of the muon at one of the two sites of the resonating situation. The fact that the measured value is considerably smaller than the calculated dipolar relaxation (0.33 μs^{-1} or 0.35 μs^{-1}) speaks against this assumption. In the experimental section II we have already questioned the localization hypothesis with the argument that the observed increase of the fraction is not plausible, if one assumes that the slow fraction is formed in a temperature-independent process in the charge exchange regime.

V. CONCLUSIONS

The intention of this paper was to find an explanation of the fast relaxing μSR signal in α-Al_2O_3. Fast relaxing μSR signals are observed also in a number of other experiments and are explained in different models.[18–21,23–25] The earlier interpretation that the signal is due to Mu^+ with subsequent delayed capture of an electron[15] could not be confirmed for Al_2O_3.[16,31,57,58] But the Mu^- and the recently proposed transition state interpretation remained a possibility. The results from the DFT-based calculations presented allowed a renewed in-depth discussion of these models.

The Mu^- model relies sensitively on the interaction of the muon with radiolytic electrons and holes from the ionization track. Reliable estimates of the corresponding reaction rates are difficult but some qualitative considerations presented in the discussion section indicate that the rates are probably too small to give an explanation of the data.

The DFT calculations revealed an effective mechanism for the formation of the bound O-Mu configuration which we assign to the transition state. The formation of the bound configuration occurs on the top of the diffusion barrier when the muonium on its trajectory migrates

close to an oxygen atom. The calculations indicate that a rather shallow energy minimum exists when the muon, Mu, approaches an oxygen atom of the lattice with the Mu−O distance of about 0.1 nm. The oxygen atom attracts the muonium and a weakly bound state with a delocalized electron distribution is formed.

A final judgment on the validity of the two models (Mu^- or transition state) is not possible with the present knowledge, but on the basis of the arguments presented here the transitional state model seems more adequate.

In addition, information on the bare muon motion has been obtained. The diamagnetic signal of the bare muon (μ^+) shows a relaxation rate which is smaller than the value expected from the nuclear dipolar interaction for the static case. This smaller value is approximately constant in the temperature range between 40 and 300 K and does not reduce to zero, thus excluding long-range diffusion of the muon in this temperature range. The reduced relaxation value is consistent with the tunneling motion of the muon between two oxygen-bound positions as predicted by Gordon *et al.*.[11]

VI. ACKNOWLEDGEMENTS

ISIS beam muon beam time allocation from the Science and Technology Facilities Council, through experiment RB1010365,[62] and the support of the ISIS muon team are gratefully acknowledged. This work was supported with funds from FEDER (Programa Operacional Factores de Competitividade COMPETE) and by national funds from FCT - Fundação para a Ciência e Tecnologia, I. P. (Portugal) under projects UIDB/04564/2020, UIDP/04564/2020 and PTDC/FIS-MAC/29696/2017.

* ruivilao@uc.pt

[1] E. R. Dobrovinskaya, L. A. Lytvynov, and V. Pishchik, *Sapphire: Material, Manufacturing, Applications*, Springer, 2009.

[2] M. Behrens, F. Studt, I. Kasatkin, S. Kühl, M. Hävecker, F. Abild-Pedersen, S. Zander, F. Girgsdies, P. Kurr, B.-L. Kniep, M. Tovar, R. W. Fischer, J. K. Nørskov, and R. Schlögl, The Active Site of Methanol Synthesis over Cu/ZnO/Al2O3 Industrial Catalysts, Science **336**, 893 (2012).

[3] A. C. Kozen, C.-F. Lin, A. J. Pearse, M. A. Schroeder, X. Han, L. Hu, S.-B. Lee, G. W. Rubloff, and M. Noked, Next-Generation Lithium Metal Anode Engineering via Atomic Layer Deposition, ACS Nano **9**, 5884 (2015).

[4] D. S. Jeong, R. Thomas, R. S. Katiyar, J. F. Scott, H. Kohlstedt, A. Petraru, and C. S. Hwang, Emerging memories: resistive switching mechanisms and current status, Rep. Prog. Phys. **75**, 076502 (2012).

[5] G. Dingemans, and W. M. M. Kessels, Status and prospects of Al_2O_3−based surface passivation schemes for silicon solar cells, Journal of Vacuum Science & Technology A **30**, 040802 (2012).

[6] M. A. Curado, J. P. Teixeira, M. Monteiro, E. F. M. R. Ribeiro, R. C. Vilão, H. V. Alberto, J. M. V. Cunha, T. S. Lopes, K. Oliveira, O. Donzel-Gargand, A. Hultqvist, S. Calderon, M. A. Barreiros, W. Chiappim, J. P. Leitão, A. G. Silva, T. Prokscha, C. Vinhais, P. A. Fernandes, and P. M. P. Salomé, Front passivation of Cu(In,Ga)Se_2 solar cells using Al_2O_3: Culprits and benefits, Applied Materials Today **21**, 100867 (2020).

[7] G. Dingemans, F. Einsele, W. Beyer, M. C. M. van de Sanden, and W. M. M. Kessels, Influence of annealing and Al_2O_3 properties on the hydrogen-induced passivation of the Si/SiO_2 interface, Journal of Applied Physics **111**, 093713 (2012).

[8] Z. Guo, F. Ambrosio, and A. Pasquarello, Extrinsic Defects in Amorphous Oxides: Hydrogen, Carbon, and Nitrogen Impurities in Alumina, Phys. Rev. Applied **11**, 024040 (2019).

[9] O. A. Dicks, J. Cottom, A. L. Shluger, and V. V. Afanas'ev, The origin of negative charging in amorphous Al2O3 films: the role of native defects, Nanotechnology **30**, 205201 (2019).

[10] M. S. Khalil, M. J. A. Stoutimore, S. Gladchenko, A. M. Holder, C. B. Musgrave, A. C. Kozen, G. Rubloff, Y. Q. Liu, R. G. Gordon, J. H. Yum, S. K. Banerjee, C. J. Lobb, and K. D. Osborn, Evidence for hydrogen two-level systems in atomic layer deposition oxides, Applied Physics Letters **103**, 162601 (2013).

[11] L. Gordon, H. Abu-Farsakh, A. Janotti, and C. G. Van de Walle, Hydrogen bonds in Al_2O_3 as dissipative two-level systems in superconducting qubits, Scientific Reports **4**, 7590 (2014).

[12] E. V. Minaĭchev, G. G. Myasishchevah, Yu. V. Obukhov, V. S. Roganov, G. I. Savel'ev, and V. G. Firsov, Paschen-Back effect for the muonium atom, Soviet Physics JETP **31**, 849 (1970).

[13] R. F. Kiefl, E. Holzschuh, H. Keller, W. Kündig, P. F. Meier, B. D. Patterson, J. W. Schneider, K. W. Blazey, S. L. Rudaz, and A. B. Denison, Decoupling of Muonium in High Transverse Magnetic Fields, Phys. Rev. Lett. **53**, 90 (1984)

[14] S. R. Kreitzman, R. F. Kiefl, D. R. Noakes, J. H. Brewer, and E. J. Ansaldo, Hyperfine Interactions **32**, 521 (1986).

[15] V. Storchak, J. H. Brewer, and G. D. Morris, Quantum transport of electronic polarons in sapphire, Phys. Rev. B **56**, 55 (1997).

[16] J. D. Brewer, J. H. Brewer, G. D. Morris, D. G. Eshchenko, and V. G. Storchak, Electric-field-induced muonium formation in sapphire, Physica B: Condensed Matter **289**, 428 (2000).

[17] S. F. J. Cox, J. L. Gavartin, J. S. Lord, S. P. Cottrell, J. M. Gil, H. V. Alberto, J. Piroto Duarte, R. C. Vilão, N. Ayres de Campos, D. J. Keeble, E. A. Davis, M. Charlton, and D. P. van der Werf, Oxide muonics: II. Modelling the electrical activity of hydrogen in wide-gap and high-permittivity dielectrics, Journal of Physics: Condensed Matter **18**, 1079 (2006).

[18] R. L. Lichti, S. F. J. Cox, K. H. Chow, E. A. Davis,

T. L. Estle, B. Hitti, E. Mytilineou, and C. Schwab, Charge-state transitions of muonium in germanium, Phys. Rev. B **60**, 1734 (1999).

[19] I. Fan, K. H. Chow, B. Hitti, R. Scheuermann, A. I. Mansour, W. A. MacFarlane, B. E. Schultz, M. Egilmez, J. Jung, Y. G. Celebi, H. N. Bani-Salameh, B. R. Carroll, J. E. Vernon, and R. L. Lichti, Influence of photoexcitation on the diamagnetic muonium states in Ge studied via their precession signatures, Phys. Rev. B **78**, 153203 (2008).

[20] R. C. Vilão, A. G. Marinopoulos, R. B. L. Vieira, A. Weidinger, H. V. Alberto, J. P. Duarte, J. M. Gil, J. S. Lord, and S. F. J. Cox, Hydrogen impurity in paratellurite $\alpha-TeO_2$: Muon-spin rotation and ab initio studies, Phys. Rev. B **84**, 045201 (2011).

[21] T. Prokscha, K. H. Chow, E. Stilp, A. Suter, H. Luetkens, E. Morenzoni, G. J. Nieuwenhuys, Z. Salman, and R. Scheuermann, Photo-induced persistent inversion of germanium in a 200-nm-deep surface region, Scientific Reports **3**, 2569 (2013)

[22] S. F. J. Cox, R. L. Lichti, J. S. Lord, E. A. Davis, R. C. Vilão, J. M. Gil, T. D. Veal, and Y. G. Celebi, The first 25 years of semiconductor muonics at ISIS, modelling the electrical activity of hydrogen in inorganic semiconductors and high-κ dielectrics, Physica Scripta **88**, 068503 (2013).

[23] R. B. L. Vieira, R. C. Vilão, H. V. Alberto, J. M. Gil, A. Weidinger, B. B. Baker, P. W. Mengyan, and R. L. Lichti, High-field study of muonium states in HfO_2 and ZrO_2, Journal of Physics: Conference Series **551**, 012048 (2014).

[24] R. B. L. Vieira, R. C. Vilão, A. G. Marinopoulos, P. M. Gordo, J. A. Paixão, H. V. Alberto, J. M. Gil, A. Weidinger, R. L. Lichti, B. Baker, P. W. Mengyan, and J. S. Lord, Isolated hydrogen configurations in zirconia as seen by muon spin spectroscopy and *ab initio* calculations, Phys. Rev. B **94**, 115207 (2016).

[25] H. V. Alberto, R. C. Vilão, R. B. L. Vieira, J. M. Gil, A. Weidinger, M. G. Sousa, J. P. Teixeira, A. F. da Cunha, J. P. Leitão, P. M. P. Salomé, P. A. Fernandes, T. Törndahl, T. Prokscha, A. Suter, and Z. Salman, Slow-muon study of quaternary solar-cell materials: Single layers and $p-n$ junctions, Phys. Rev. Materials **2**, 025402 (2018).

[26] T. Prokscha, E. Morenzoni, D. G. Eshchenko, N. Garifianov, H. Glückler, R. Khasanov, H. Luetkens, and A. Suter, Formation of Hydrogen Impurity States in Silicon and Insulators at Low Implantation Energies, Phys. Rev. Lett. **98**, 227401 (2007).

[27] R. C. Vilão, R. B. L. Vieira, H. V. Alberto, J. M. Gil, and A. Weidinger, Role of the transition state in muon implantation, Phys. Rev. B **96**, 195205 (2017).

[28] P. Hohenberg, and W. Kohn, Inhomogeneous Electron Gas, Phys. Rev. **136**, B864 (1964).

[29] W. Kohn, and L. J. Sham, Self-Consistent Equations Including Exchange and Correlation Effects, Phys. Rev. **140**, A1133 (1965).

[30] B. Patterson, Muonium states in semiconductors, Reviews of Modern Physics **60**, 69 (1988).

[31] S. F. J. Cox, Muonium as a model for interstitial hydrogen in the semiconducting and semimetallic elements, Reports on Progress in Physics **72**, 116501 (2009).

[32] M. C. Lynch, S. P. Cottrell, P. J. C. King, and G. H. Eaton, Measuring small samples at the ISIS muon source, Physica B: Condensed Matter **326**, 270 (2003).

[33] F. L. Pratt, WIMDA: a muon data analysis program for the Windows PC, Physica B: Condensed Matter **289-290**, 710 (2000).

[34] R. C. Vilão, H. V. Alberto, J.P. Duarte, J. M. Gil, A. Weidinger, N. Ayres de Campos, R. L. Lichti, K. H. Chow, and S. F. J. Cox, Muonium spectroscopy in ZnSe: Metastability and conversion, Phys. Rev. B **72**, 235203 (2005).

[35] R. C. Vilão, H. V. Alberto, J. M. Gil, and A. Weidinger, Thermal spike in muon implantation, Physical Review B **99**, 195206 (2019).

[36] P. E. Blöchl, Projector augmented-wave method, Phys. Rev. B **50**, 17953 (1994).

[37] G. Kresse, and D. Joubert, From ultrasoft pseudopotentials to the projector augmented-wave method, Phys. Rev. B **59**, 1758 (1999).

[38] G. Kresse, and J. Hafner, Ab initio molecular dynamics for liquid metals, Phys. Rev. B **47**, 558 (1993).

[39] G. Kresse, and J. Hafner, Ab initio molecular-dynamics simulation of the liquid-metal–amorphous-semiconductor transition in germanium, Phys. Rev. B **49**, 14251 (1994).

[40] G. Kresse, and J. Furthmüller, Efficient iterative schemes for ab initio total-energy calculations using a plane-wave basis set, Phys. Rev. B **54**, 11169 (1996).

[41] J. P. Perdew, K. Burke, and M. Ernzerhof, Generalized Gradient Approximation Made Simple, Phys. Rev. Lett. **77**, 3865 (1996).

[42] J. Heyd, and G. E. Scuseria, Efficient hybrid density functional calculations in solids: Assessment of the Heyd–Scuseria–Ernzerhof screened Coulomb hybrid functional, The Journal Chem. Phys. **121**, 1187 (2004).

[43] J. Paier, M. Marsman, K. Hummer, G. Kresse, I. C. Gerber, and J. G. Angyan, Screened hybrid density functionals applied to solids, The Journal Chem. Phys. **124**, 154709 (1996).

[44] M. L. Kronberg, Plastic deformation of single crystals of sapphire: Basal slip and twinning, Acta Metall. **5**, 507 (1957).

[45] R. E. Newnham, and Y. M. de Haan, Refinement of the α-Al_2O_3, Ti_2O_3, V_2O_3 and Cr_2O_3 structures, Zeitschr. Kristallographie **117**, 235 (1962).

[46] R. H. French, Electronic Band Structure of Al_2O_3, with Comparison to AlON and AlN, J. Am. Ceram. Soc. **73**, 477 (1990).

[47] R. H. French, D. J. Jones, and S. Loughin, Interband Electronic Structure of α-Alumina up to 2167 K, J. Am. Ceram. Soc. **77**, 412 (1994).

[48] M. Betzinger, C. Friedrich, and S. Blügel, Hybrid functionals within the all-electron FLAPW method: Implementation and applications of PBE0, Phys. Rev. B **81**, 195117 (2010).

[49] A. G. Marinopoulos, and M. Grüning, Local-field and excitonic effects in the optical response of α-alumina, Phys. Rev. B **83**, 195129 (2011).

[50] G. Makov, and M. C. Payne, Periodic boundary conditions in ab initio calculations, Phys. Rev. B **51**, 4014 (1995).

[51] M. Schubert, T. E. Tiwald, and C. M. Herzinger, Infrared dielectric anisotropy and phonon modes of sapphire, Phys. Rev. B **61**, 8187 (2000).

[52] H. Jónsson, G. Mills, K. W. Jacobsen, *Nudged Elastic Band Method for Finding Minimum Energy Paths of Transitions* in *Classical and Quantum Dynamics in Condensed Phase Simulations*, B.J. Berne, G. Ciccotti and D. F. Coker, eds., World Scientific, 1998, 385-404.

[53] K. Szász, T. Hornos, M. Marsman, and A. Gali, Hyperfine coupling of point defects in semiconductors by hybrid

density functional calculations: The role of core spin polarization, Phys. Rev. B **88**, 075202 (2013).

[54] J.M. Spaeth and H. Overhof, *Point Defects in Semiconductors and Insulators*, Vol. 51 of *Springer Series in Materials Science*, Springer-Verlag, Berlin Heidelberg, 2003.

[55] H. Li, and J. Robertson, Behaviour of hydrogen in wide band gap oxides, Journal of Applied Physics **115**, 203708 (2014).

[56] C. G. Van de Walle, and P. E. Blöchl, First-principles calculations of hyperfine parameters, Phys. Rev. B **47**, 4244 (1993).

[57] R. C. Vilão, H. V. Alberto, R. B. L. Vieira, J. M. Gil, and A. Weidinger, Reply to "Comment on 'Role of the transition state in muon implantation' and 'Thermal spike in muon implantation"', Phys. Rev. B **101**, 077202 (2020).

[58] J. H. Brewer, V. G. Storchak, G. D. Morris, and D. Eshchenko, Comment on "Role of the transition state in muon implantation" and "Thermal spike in muon implantation", Phys. Rev. B **101**, 077201 (2020).

[59] A. G. Marinopoulos, First-principles study of hydrogen configurations at the core of a high-angle grain boundary in cubic yttria-stabilized zirconia, Journal of Physics: Condensed Matter **26**, 025502 (2014).

[60] J. H. Van Vleck, The Dipolar Broadening of Magnetic Resonance Lines in Crystals, Phys. Rev. **74**, 1168 (1948).

[61] O. Hartmann, Quadrupole Influence on the Dipolar-Field Width for a Single Interstitial in a Metal Crystal, Phys. Rev. Lett. **39**, 832 (1977).

[62] R. C. Vilão, J. M. Gil, S. P. Cottrell, J. S. Lord, J. Piroto Duarte, H. V. Alberto, S. F. J. Cox, and A. Weidinger, Muonium in widegap oxides, STFC ISIS Neutron and Muon Source (2010), https://data.isis.stfc.ac.uk/doi/investigation/24081085.